

Investigating the role of undercoordinated Pt sites at the surface of layered PtTe₂ for methanol decomposition

Received: 23 May 2023

Accepted: 8 January 2024

Published online: 22 January 2024

 Check for updates

Jing-Wen Hsueh¹, Lai-Hsiang Kuo¹, Po-Han Chen², Wan-Hsin Chen³, Chi-Yao Chuang³, Chia-Nung Kuo^{4,5}, Chin-Shan Lue^{4,5,6}, Yu-Ling Lai⁷, Bo-Hong Liu⁷, Chia-Hsin Wang⁷, Yao-Jane Hsu⁷, Chun-Liang Lin³✉, Jyh-Pin Chou⁸✉ & Meng-Fan Luo¹✉

Transition metal dichalcogenides, by virtue of their two-dimensional structures, could provide the largest active surface for reactions with minimal materials consumed, which has long been pursued in the design of ideal catalysts. Nevertheless, their structurally perfect basal planes are typically inert; their surface defects, such as under-coordinated atoms at the surfaces or edges, can instead serve as catalytically active centers. Here we show a reaction probability > 90 % for adsorbed methanol (CH₃OH) on under-coordinated Pt sites at surface Te vacancies, produced with Ar⁺ bombardment, on layered PtTe₂ – approximately 60 % of the methanol decompose to surface intermediates CH_xO (x = 2, 3) and 35 % to CH_x (x = 1, 2), and an ultimate production of gaseous molecular hydrogen, methane, water and formaldehyde. The characteristic reactivity is attributed to both the triangular positioning and varied degrees of oxidation of the under-coordinated Pt at Te vacancies.

Two-dimensional transition metal dichalcogenides (TMDs) have attracted considerable interest, owing to their distinctive electronic properties^{1–8} and highly tunable surface reactivity^{9–16}. TMDs, by virtue of their two-dimensional structures, could provide the largest active surface for reactions with minimal materials consumed, which has long been a goal in the design of ideal catalysts. Structurally perfect basal planes of TMDs are typically inert whereas their surface defects, such as unsaturated coordinative atoms at the surfaces or edges, become catalytically active centers. Many studies on MoS₂, one of the most developed TMDs, have demonstrated that by controlling the density of sulfur vacancies (active centers) at MoS₂ surface, its reactivity toward varied reactions can be manipulated^{13–21}. For instance, the sulfur vacancies at MoS₂ surface,

in spite of varied generation approaches (plasma¹⁰, ion bombardment¹³ or chemical etching¹⁴), facilitated hydrogen evolution reaction, through the mechanism involved with altered surface electronic structures and boosted electric conductivity^{10,13,14}. Pt-based catalysts, including single crystals, nanoclusters, alloys, and electrodes, have been extensively investigated in both heterogeneous catalysis and electrocatalysis, because of their superior catalytic properties^{22–42}. Nevertheless, the catalytic properties of Pt-based TMDs have been little explored^{11,43–45}, even though they could possess better chemical and structural stability than commercial Pt-based catalysts such as supported Pt nanoclusters. The present study aims to shed light on the catalytic properties of Pt-based TMDs and their potential as catalysts.

¹Department of Physics, National Central University, No. 300 Jhongda Rd., Jhongli District, Taoyuan City 320317, Taiwan. ²Department of Materials Science and Engineering, National Tsing Hua University, 101, Section 2 Kuang-Fu Road, Hsinchu 300044, Taiwan. ³Department of Electrophysics, National Yang Ming Chiao Tung University, No. 1001 University Rd., Hsinchu 300039, Taiwan. ⁴Department of Physics, National Cheng Kung University, No. 1 University Rd., Tainan 701, Taiwan. ⁵Taiwan Consortium of Emergent Crystalline Materials, National Science and Technology Council, Taipei 10601, Taiwan. ⁶Program on Key Materials, Academy of Innovative Semiconductor and Sustainable Manufacturing, National Cheng Kung University, Tainan 701, Taiwan. ⁷National Synchrotron Radiation Research Center, 101 Hsin-Ann Rd., Hsinchu Science Park, Hsinchu 300092, Taiwan. ⁸Department of Physics, National Changhua University of Education, No. 1, Jin-De Rd., Changhua 50007, Taiwan. ✉e-mail: clin@nycu.edu.tw; jpchou@cc.ncue.edu.tw; mfl28@phy.ncu.edu.tw

We studied the decomposition of methanol (methanol- d_4) on layered PtTe_2 with various surface-probe techniques under both ultrahigh-vacuum (UHV) and near-ambient-pressure (NAP) conditions. Methanol (CH_3OH) decomposition serves as the principal reaction in direct methanol fuel cells (DMFCs), a promising device that converts methanol efficiently to electricity^{46–52}, and the liberation of hydrogen from the decomposition leads to viable generation of hydrogen, another clean source of energy^{53,54}. PtTe_2 , as a group-10 TMD material, draws much attention for its tunable bandgap, high charge mobility, and ultrahigh air stability^{1,3,5–7,11,43,44}, but its surface reactivity is little understood. We generated the surface defects on PtTe_2 and controlled their concentration with Ar ion (Ar^+) bombardment. The surface structures of PtTe_2 were characterized using scanning tunneling microscopy (STM) and synchrotron-based photoelectron spectroscopy (PES), while the reactions, intermediates, and products, were monitored using PES, near-ambient-pressure photoelectron spectroscopy (NAP-PES) and near-ambient-pressure mass spectroscopy (NAP-MS). We also performed calculations based on density functional theory (DFT) to explore the mechanisms in detail.

The results showed that under-coordinated Pt (denoted as Pt_{uc}) at the PtTe_2 surface served as active sites for the reaction. Both dehydrogenation and C–O bond scission occurred for adsorbed methanol on the Pt_{uc} sites, leading to the formation of CH_xO^* ($x = 2$ and 3; * denotes adsorbates) and CH_x^* ($x = 1$ and 2) as major intermediates and finally production of gaseous molecular hydrogen, methane, water, and formaldehyde via various processes. Gaseous formaldehyde ($\text{CH}_2\text{O}_{(\text{g})}$) was rarely observed from methanol decomposition on either Pt single crystals or supported Pt nanoclusters; meanwhile, CO^* (or $\text{CO}_{(\text{g})}$), a common product from Pt-based catalysts^{22–26,30,33–36,42}, was not produced in the present reaction; the pathway of C–O bond scission in the present reaction accounted for a significant proportion (reflected on a considerable quantity of produced CH_x^*), which also contrasts with its minor role on supported Pt clusters³⁴. The catalytic nature of Pt_{uc} sites on PtTe_2 thus differs from that of typical Pt-based catalysts. Moreover, the reactivity depended notably on the Pt_{uc} concentration. At a small Pt_{uc} concentration ($\leq 10\%$), methanol on the Pt_{uc} at surface Te vacancies, the dominating surface defects, decomposed at a great probability ($> 90\%$). With increased Pt_{uc} concentration (10–20%), the probability decreased as the probability of decomposition to CH_xO^* was selectively decreased, attributed to structurally different Pt_{uc} generated by extended Ar^+ bombardment. Nevertheless, in either case, the reaction probability ($\geq 80\%$) exceeds those on Pt single crystals^{22,25} and supported Pt clusters³⁴. We propose, with the support of DFT modeling, that both structural and electronic effects play essential roles in determining the observed catalytic properties. These results suggest that a PtTe_2 surface with the Pt_{uc} at surface Te vacancies can serve as a superior catalyst for methanol decomposition; its catalytic selectivity can be controlled with the surface structures manipulated by varied Ar^+ bombardment.

Results

Structural characterization with STM and PES

We utilized STM to characterize the surface structures of layered PtTe_2 before and after the treatment of Ar^+ bombardment. The as-cleaved surface was generally very flat and had few defects, as illustrated in Fig. 1a; the hexagonally arranged white spots were topmost Te atoms imaged, and several types of intrinsic defects observed previously with STM⁵, such as Te and Pt vacancies, were also observed in the present sample (Fig. S1). After controlled Ar^+ bombardment, the surface Te vacancies were evidently increased, together with few small clusters on the surface; the size of the vacancies varied from single- to multiple-Te vacancies (Fig. 1b) and the proportion of larger vacancies increased with the bombardment time (Fig. S1). Continuing to increase either the bombardment time or the Ar^+ kinetic energy generated more not only

the surface Te vacancies but also structural variations, such as island edges and re-deposited atoms (Fig. 1c, d). With the aim of correlating structures with reactivity, we chose a kinetic energy of 0.5 keV for incident Ar^+ and a reduced Ar^+ dosage (the sample current multiplied by bombardment time) to control structural complexity for reaction experiments – the Te vacancies were produced as the main surface defects while the surface crystallinity (monitored with the RHEED measurements, Fig. S2) was largely sustained.

Fig. 1e–h exemplify a high-resolution image for two single-Te vacancies and the corresponding line profile across one of the vacancies. The vacancy depth about 0.1 nm (Fig. 1f), similar to that of an intrinsic Te vacancy at the surface (Fig. S1), and the well overlap of the top Te atoms and vacancies in the model with the imaged ones (Fig. 1g) suggest that the vacancies were formed by the removal of the topmost Te atoms, i.e., the surface Te vacancies. As the positions of the surface Te atoms neighboring the vacancies remained nearly unchanged (Fig. 1g) and as they were mainly bonded to the underlying Pt, the generation of these Te vacancies altered little the positions of underlying Pt atoms. The well match of the STM image with the DFT-simulated one (Fig. 1h), produced based on the vacancy model in Fig. 1g, corroborates the vacancy structure. Small Ar^+ dosages removed mainly the surface Te while left the underlying Pt atoms unaltered. Our DFT modeling for the reactions discussed below also adds weight to the argument. The small clusters in Fig. 1b likely correspond to re-deposited atoms (0.15 nm, one-atom high) after Ar^+ bombardment. As they were much fewer than the surface Te vacancies at small Ar^+ dosages, for which the reaction experiments were primarily performed, their contribution to the observed reactions was considered limited even though they could initiate or assist (as adsorption sites) reactions.

Our PES spectra further characterized these surface defects observed with STM. Fig. 2a exemplifies the comparison of the PES spectra of Pt 4f core level for the layered PtTe_2 as cleaved and bombarded by Ar^+ . The spectrum from as-cleaved PtTe_2 (upper panel of Fig. 2a) shows a doublet, Pt 4f_{5/2} and Pt 4f_{7/2}, centered at the binding energies (BE) 75.9 and 72.6 eV respectively, which corresponds to intact Pt–Te chemical bonds in PtTe_2 . Meanwhile, the PES spectrum from Ar^+ -bombarded PtTe_2 shows an additional feature at a BE slightly smaller than that of the main Pt feature, i.e., at 71.8 eV for Pt 4f_{7/2} and 75.1 eV for Pt 4f_{5/2} (indicated by red fitted curves in the bottom panel). The smaller BE for Pt 4f implies less oxidized Pt, corresponding to under-coordinated Pt (Pt_{uc}), at the PtTe_2 surface and therefore the removal of Te atoms by Ar^+ bombardment. In contrast, the Te 4d signals were insensitive to the removal of neighboring Te atoms – the line shape of Te 4d doublet altered little after Ar^+ bombardment (Fig. 2b), since the surface Te is mainly bonded to the underlying Pt. Both the Pt 4f and Te 4d lines from Ar^+ -bombarded PtTe_2 shifted negatively (approximately 0.1 eV as shown in Fig. 2a, b), likely because the bombardment induced a band-bending effect. As the spectral features for varied Ar^+ dosages are similar despite varied intensities of the Pt_{uc} features (Fig. S3), the Pt_{uc} signals correspond to the Pt_{uc} at surface Te vacancies (denoted as $\text{Pt}_{\text{uc}}\text{-Vac}$) and also to those at other surface defects (denoted as $\text{Pt}_{\text{uc}}\text{-Ex}$) generated by greater Ar^+ dosages. Our experiments show that the number or concentration of Pt_{uc} can be controlled with Ar^+ dosage and Ar^+ kinetic energy. Fig. 2c plots the ratio of the Pt_{uc} and total Pt signals (denoted as $\text{Pt}_{\text{uc}}/\text{Pt}$), measured by the integrated intensities of the red and black fitted curves (Fig. 2a), as a function of the Ar^+ dosage. The $\text{Pt}_{\text{uc}}/\text{Pt}$ ratio increased almost in a linear fashion with the Ar^+ dosage, despite varied Ar^+ kinetic energies. As about 90% of the Pt signals came from the top two PtTe_2 bilayers (according to the escape depth of the Pt 4f photoelectrons) and as Ar^+ bombardment at a small dosage removed primarily the surface Te (Fig. 1), each $\text{Pt}_{\text{uc}}/\text{Pt}$ ratio corresponds to a derivable concentration of surface Pt_{uc} . Notably, the rate of increase of the $\text{Pt}_{\text{uc}}/\text{Pt}$ ratio depended on the Ar^+ kinetic energy, since the cross-section of removing surface}}}}

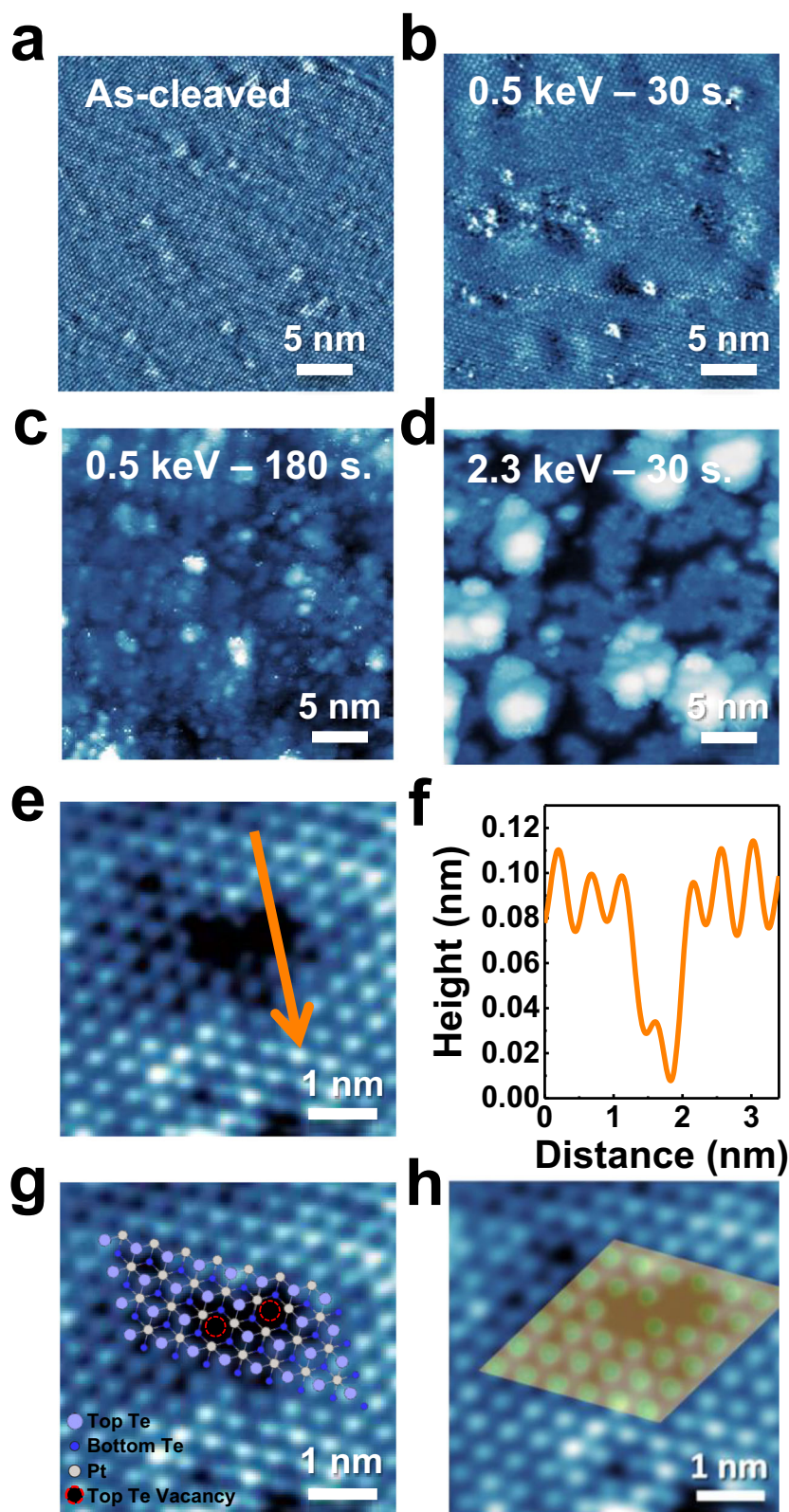


Fig. 1 | Characterization of surface structures of layered PtTe₂ with STM. STM images for layered PtTe₂ **a** as-cleaved ($V_s = -250$ mV, $I_t = 1.35$ nA) and bombarded by Ar⁺ with **b** 0.5 keV for 30 sec. ($V_s = -150$ mV, $I_t = 1.20$ nA) and **c** 180 sec., and with **d** 2.3 keV for 30 sec. ($V_s = -500$ mV, $I_t = 2.90$ nA); **e** the high-resolution image of two single-Te vacancies, **f** the line profile across a single-Te vacancy, **g** the overlap of the two single-Te vacancies model with the imaged ones and **h** the

match of the STM image with the DFT-simulated one produced based on the vacancy model in (**g**). In **g**, light blue, blue and grey balls denote top, bottom Te and Pt atoms in the topmost PtTe₂ bilayer; the dash-line circles denote single-Te vacancies. In **h**, green balls denote the simulated images for the top Te atoms; the simulated image was derived with bias -0.1 V while the images obtained with -0.5 - -0.1 V were similar.

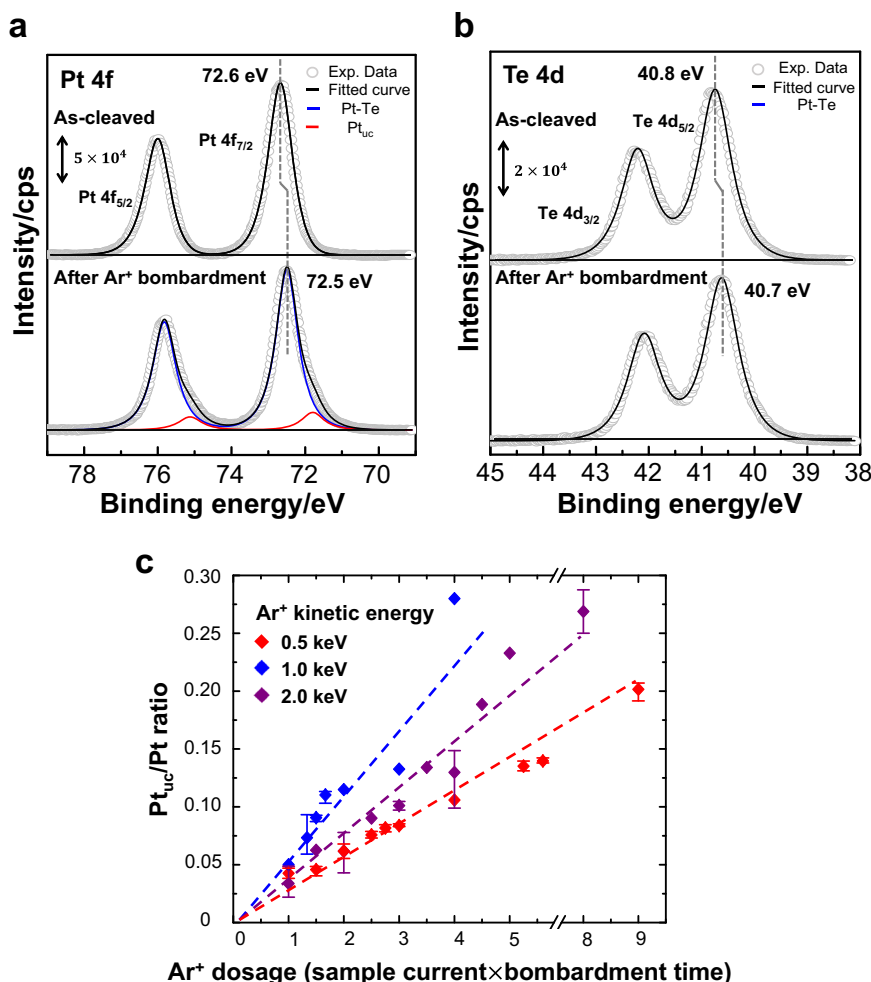


Fig. 2 | Characterization of surface structures of layered PtTe₂ with PES. PES spectra of **a** Pt 4f and **b** Te 4d core levels from layered PtTe₂ as cleaved and bombarded by Ar⁺ (0.5 keV, 3 mins); **c** ratios of integrated intensities of Pt_{uc} to Pt 4f lines as a function of Ar⁺ dosages. In **a** and **b**, gray circles denote the spectra and black lines the sum of fitted curves; the signals from intact Pt and under-

coordinated Pt (Pt_{uc}) in the layered PtTe₂ are fitted with blue and red lines, respectively. In **c**, the Ar⁺ dosages were calculated by sample current multiplied by sputtering time; the data obtained with Ar⁺ kinetic energies of 0.5, 1.0, and 2.0 keV were represented by red, blue, and purple rhombuses respectively in the plot, and the error bars indicate the reproducibility.

Te varied with the Ar⁺ kinetic energy. The Ar⁺ at 0.5 keV was chosen to prepare the sample, as it exhibited the best controllability in producing small Pt_{uc} concentrations (small Pt_{uc}/Pt ratios), warranting the surface Te vacancies as the dominating surface defects for catalytic studies (Fig. S1). Our reaction experiments were primarily performed on the PtTe₂ with Pt_{uc}/Pt ratios ≤ 0.13 (Ar⁺ dosage ≤ 4.5, Fig. 2c), corresponding to the Pt_{uc} concentration ≤ 20 %; the Ar⁺ dosages (0.5 keV) at 1 and 6 in Fig. 2c produced the surfaces resembling those shown in Fig. 1b, c respectively.

Methanol decomposition monitored with PES, NAP-PES and NAP-MS

The methanol reactions were characterized primarily by PES spectra; with the spectra, we monitored the evolution of surface species with temperature and Pt_{uc} concentrations. Fig. 3a, b compare the C 1s spectra for methanol adsorbed on as-cleaved and Ar⁺-bombarded PtTe₂ (Pt_{uc}/Pt ratio = 0.07) at 145 K and annealed stepwise to selected temperatures. The dominant feature at 145 K on either surface, centered about 286.5 eV, is assigned to the C 1s line of monolayer methanol adsorbed on PtTe₂ (top in Fig. 3a, b), since multilayer methanol desorbed near 130 K^{34,56,57}. On the as-cleaved PtTe₂ surface, the methanol signals decreased with increased temperature and vanished at 200 K, reflecting the desorption of methanol (Fig. 3a). In contrast, on the PtTe₂ with a number of surface Pt_{uc} produced by Ar⁺

bombardment, new features grew at 283.8 – 285.1 eV above 160 K, at the expense of attenuating methanol feature at 286.5 eV (Fig. 3b). The results suggest that with increased temperature, a fraction of methanol desorbed whereas the other fraction decomposed and produced new carbon species. As the as-cleaved PtTe₂ has very limited surface defects, the contrasting results indicate that the structurally perfect basal plane of layered PtTe₂ is catalytically inert but the surface Pt_{uc}, mostly at the Te vacancies (Fig. 1b, e), i.e. Pt_{uc}-Vac, are reactive toward methanol decomposition. The products at elevated temperature consisted of three carbon species: CH_xO* (x = 1-3), CH_x* (x = 1-3) and atomic carbon (C*), corresponding to the C 1s lines centered at 285.1⁵⁸⁻⁶⁴, 283.8⁶⁵⁻⁶⁷ and 284.2 eV (Fig. S4a), respectively. CO* was not expected because our adsorption experiments showed no CO adsorbed on such a defective PtTe₂ surface even at 145 K. Fig. 3c, d exemplify the fits to the C 1s lines (at 180 and 260 K) with characteristic fitted curves representing C 1s signals from adsorbed monolayer methanol and the proposed products. CH_xO* (red curve in Fig. 3c, d) and CH_x* (blue) were the primary products at 160 – 260 K but C* became notable above 260 K, implying that further decomposition of CH_xO* and/or CH_x* occurred at elevated temperature. Fig. 3e plots the integrated intensities of these fitted C 1s curves, used to measure the quantities of produced CH_xO*, CH_x*, and C*, as a function of temperature. The produced CH_xO* (red circles) and CH_x* (blue) increased to maxima near 180 K and decreased at even higher temperatures, whereas C*

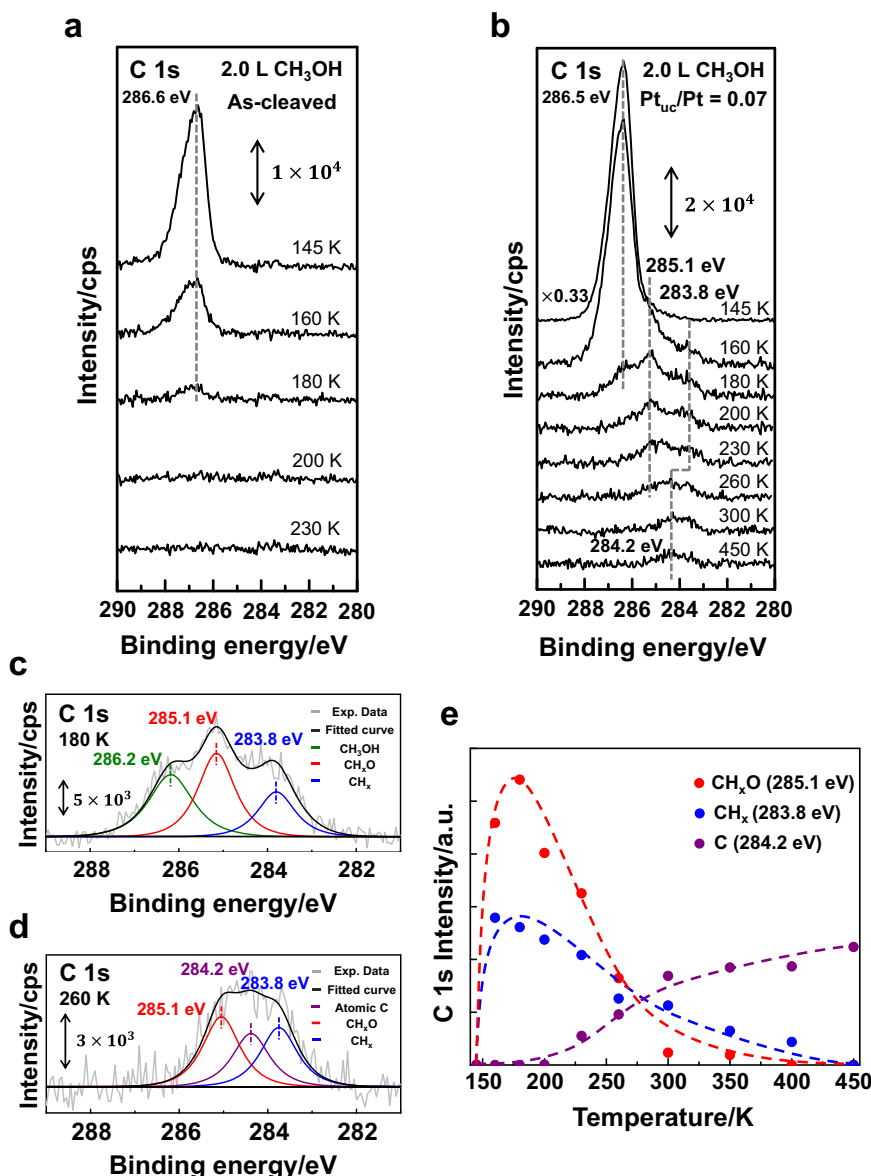


Fig. 3 | Reactions of methanol adsorbed on PtTe₂ monitored with PES. PES spectra of C 1s core level for methanol (4.0 and 2.0 L) adsorbed on **a** as-cleaved and **b** Ar⁺-bombarded PtTe₂ at 145 K and annealed stepwise to selected temperatures; the illustration fits the spectra obtained at **c** 180 and **d** 260 K; **e** the integrated intensities of the fitted curves representing CH_xO* (red circles), CH_x* (blue and C* (purple) signals as a function of temperature. In **c** and **d**, gray lines denote the spectra and black ones the sum of fitted curves; adsorbed methanol, CH_xO*, CH_x*, and C* signals are fitted with green, red, blue, and purple lines, respectively. The dash lines in (**e**) are the guidance for eyes only.

(purple) began to emerge above 200 K and became the major species at and above 300 K. The formation of CH_xO* and CH_x* indicates that dehydrogenation and C-O bond scission, the two competing processes of methanol decomposition^{30,34,35,68}, were both catalytically activated at such low temperature on the surface Pt_{uc} sites. A fraction of CH_xO* and CH_x* must have desorbed at elevated temperature, since the quantity of the remaining C* was not comparable to that of the produced CH_xO* and CH_x* (Fig. 3e). Our NAP experiments presented below indicate that the desorbing carbon species consisted largely of CH₂O_(g) and CH_{4(g)}.

To reveal how the catalytic properties of PtTe₂ surface vary with the concentration of surface Pt_{uc}, we plot the probabilities of conversion of adsorbed monolayer methanol to CH_xO* (red circles) and CH_x* (blue) as a function of the concentration of surface Pt_{uc}, shown in Fig. 4a. The conversion probability was derived from the ratio of the C 1s intensities of CH_xO* (or CH_x*) to monolayer methanol (145 K); the former was measured at 180 K because the maximum quantity of CH_xO* (or CH_x*) was produced around 180 K; only monolayer

methanol was considered because it was directly in contact with the PtTe₂ surface. The concentration of surface Pt_{uc} was estimated according to the measured Pt_{uc}/Pt ratios (Fig. 2), as mentioned above; the percentage corresponds to the fraction of Pt_{uc} in the total amount of Pt in the top PtTe₂ bilayer. For CH_x* (blue circles), the conversion probability of monolayer methanol increased almost in linear proportion to the Pt_{uc} concentration, corroborating that Pt_{uc} served as reactive sites for the C-O bond scission. Nevertheless, the trend becomes complicated for CH_xO* (red). The conversion probability increased linearly at a Pt_{uc} concentration ≤ 10 %, while became saturated (10 - 20 %) or even decreased at a greater Pt_{uc} concentration (> 20 %). At greater Pt_{uc} concentrations (> 10 %) the Pt_{uc} structurally different from Pt_{uc}-Vac had grown and accounted for a fraction of total Pt_{uc}, although they were not resolved in the Pt 4f spectra. Such Pt_{uc} corresponded to Pt_{uc}-Ex; they possessed different catalytic properties so initiated a separate reaction pathway, for which the C-O bond scission was more facilitated so CH_xO* became unstable and decreased.

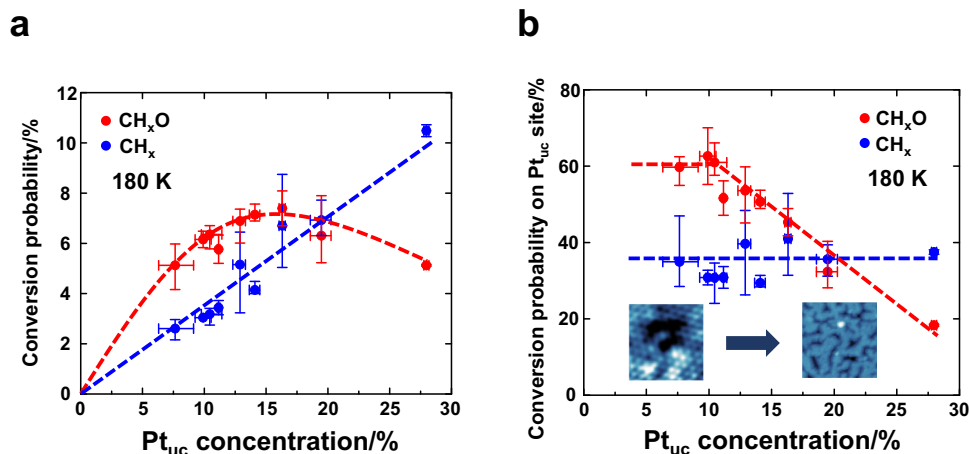


Fig. 4 | Varied reaction probabilities of methanol adsorbed on PtTe₂ surface with Pt_{uc} sites. Probabilities of conversion to CH_xO* (red circles) and CH_x* (blue) of monolayer methanol adsorbed on **a** PtTe₂ surface, and those on **b** Pt_{uc} sites as a function of the concentration of surface Pt_{uc}. The dash lines are drawn to guide eyes

only and the error bars indicate reproducibility. The insets (STM images) in **(b)** indicate the structural evolution with the concentration of surface Pt_{uc} (Ar⁺ dosages).

The conversion probability of methanol adsorbed on the Pt_{uc} sites (denoted as methanol/Pt_{uc}) as a function of the Pt_{uc} concentration shows clearly the evolving catalytic selectivity (Fig. 4b). The fraction of methanol/Pt_{uc} in total monolayer methanol was estimated to be that of Pt_{uc} in total amount of Pt in the top PtTe₂ bilayer (the Pt_{uc} concentration), by assuming that monolayer methanol adsorbed uniformly on the PtTe₂ surface. As shown in Fig. 4b, the conversion probability of methanol/Pt_{uc} to CH_x* varied little with the Pt_{uc} concentration, remaining near 35%; in contrast, that to CH_xO* was approximately 60% at a Pt_{uc} concentration ≤ 10% but decreased continuously at a Pt_{uc} concentration > 10%. The observation does not simply suggest that the formation of CH_xO* (dehydrogenation) was structure-sensitive whereas that of CH_x* (C-O bond scission) was not^{69–71} because the productions of these two intermediates were not necessarily separate – CH_x* could be produced largely via the C-O bond scission of CH_xO*. Besides, both the dehydrogenation and C-O bond scission were considered sensitive to structures^{69–71}. The present result is likely due to enhanced C-O bond scission, which decreases CH_xO* but increases CH_x*, and obstructed dehydrogenation, which decreases both CH_xO* and CH_x*, on the Pt_{uc}-Ex sites mentioned above. Our STM measurements show that at a greater Ar⁺ dosage (Pt_{uc} concentration > 10%), the generated surface defects include not only the Te vacancies (Fig. 1b) but also other defects, such as edges of PtTe₂ patches (islands) and Pt-Te nanoclusters formed by nucleation of redeposited Pt and Te (exemplified in Fig. 1c and Fig. S4b). We thus associated the Pt_{uc}-Ex with the Pt_{uc} at these two surface defects. Nevertheless, we note that the total reaction probability was remarkably great – about 95% at a Pt_{uc} concentration ≤ 10% and remaining greater than 80% even at a concentration near 20%. In either case, the reaction probability exceeded that for methanol on either Pt single-crystal surfaces (10%)^{22,25} or supported Pt clusters (60–70%)³⁴. Additionally, the probability of conversion to CH_x* (35%) was also evidently greater than that on Pt clusters (<10%)³⁴; the C-O bond scission pathway apparently played an important role in the present reaction.

The above experiments demonstrate that the catalytic reactivity of layered PtTe₂ is controllable by the surface Pt_{uc} under UHV conditions. To unveil their catalytic performance under “real-world” conditions⁷², we investigated methanol reactions on layered PtTe₂ near ambient pressure. Fig. 5a exemplifies the NAP-PES spectra of C 1s core level from PtTe₂ bombarded by Ar⁺ (Pt_{uc}/Pt ratio = 0.10) and subsequently exposed stepwise to selected pressures of methanol at 300 K; 300 K was used because the desorption and further decomposition of

products (intermediates) already occurred (Fig. 3). The as-bombarded PtTe₂ surface was free of carbon contamination, indicated by the absence of C 1s signals (the bottom of Fig. 5a); increasing methanol pressure to 10^{−4} mbar, a small C 1s line arose around 284.2 eV and continued to grow with increased pressure; at 10^{−3} mbar and above, a shoulder centered about 283.0 eV (Fig. 5a,b) also grew. The former is assigned to C*, while the latter to CH_x*, both of which resulted from decomposed methanol on PtTe₂. The reactions must have occurred on the surface Pt_{uc} sites (largely Pt_{uc}-Vac sites at this small Pt_{uc} concentration) as the experiments on as-cleaved PtTe₂ (with scarce surface Pt_{uc}), as a comparison, showed negligible C 1s signals. This observation agrees with that on the Ar⁺-bombarded PtTe₂ surface under UHV conditions, in which C* and CH_x* were primary remaining species on the surface at 300 K (Fig. 3e). These C 1s signals increased with methanol pressure, since more methanol decomposed on the PtTe₂ surface at greater methanol pressures. They decreased at 0.1 mbar (second from the top in Fig. 5a) as the photoelectrons were attenuated by the increased pressure; at such a great pressure, the C 1s feature resulting from gaseous methanol also appeared at 288.5 eV^{35,73}. Notably, the ratio of CH_x* to C* signals increased with methanol pressure but altered little with the decreasing pressure from 0.1 to 10^{−7} mbar. The ratio was affected little by the pressure-induced signal attenuation but determined by the composition of carbon species on the surface. The fraction of CH_x* in total surface carbon species became greater at a greater pressure or C* concentration. We speculate that a greater C* concentration at the Pt_{uc} sites suppressed the dehydrogenation of CH_x* by altering the electronic properties of Pt_{uc} and/or adsorption configurations of CH_x*.

The corresponding gaseous products from the methanol reactions near ambient pressure were monitored with NAP-MS. Fig. 5c exemplifies the observed main products, including D_{2(g)}, D_{2O(g)}/CD_{4(g)} and CD_{2O(g)}, from Ar⁺-bombarded PtTe₂ (Pt_{uc}/Pt ratio = 0.10) at 300 K exposed to methanol-d₄ (CD₃OD) at varied pressures. Instead of methanol, methanol-d₄ was used because these isotopic variants have similar chemical properties, such as the activation for desorption and decomposition (determined from their electronic structures), but methanol-d₄ gave clearer signals of molecular deuterium (D₂), an essential product to reveal the reaction mechanisms, in desorption experiments. These three desorbing species increased generally with methanol-d₄ pressure, consistent with the above NAP-PES experiments, as more methanol-d₄ interacted with the Pt_{uc} at a higher methanol-d₄ pressure. D_{2(g)} came from recombinative desorption of D*, while D* was produced from dehydrogenated CD₃OD*,

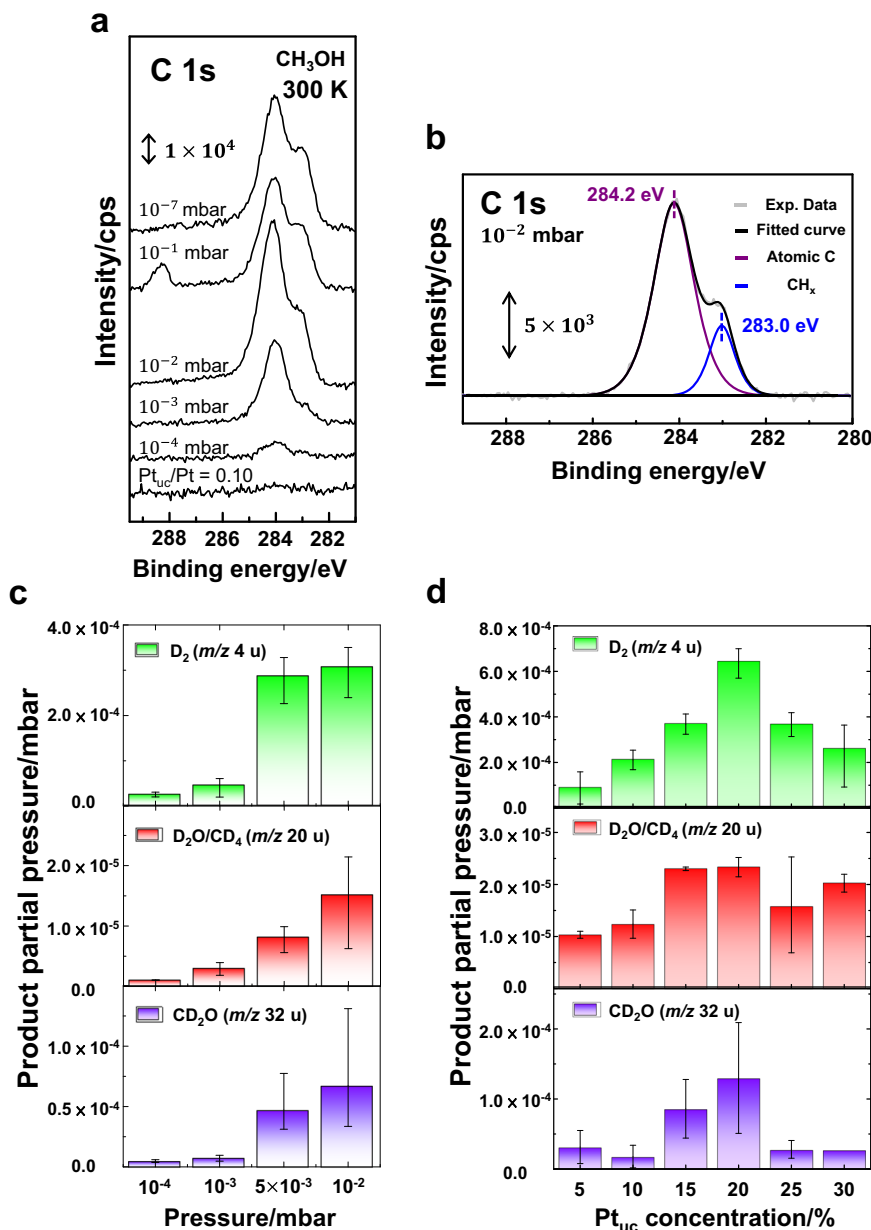


Fig. 5 | Reactions of methanol on PtTe₂ under NAP conditions monitored with NAP-PES and NAP-MS. NAP-PES spectra of **a** C 1s core level from Ar⁺-bombarded PtTe₂ (Pt_{uc}/Pt ratio 0.10) exposed to varied pressures of methanol, as indicated, at 300 K; **b** the illustration of the fit to the spectrum obtained at methanol pressure 10⁻² mbar; the production of D_{2(g)} (*m/z* 4 u), D₂O_(g)/CD_{4(g)} (*m/z* 20 u) and CD₂O_(g)

(*m/z* 32 u) from PtTe₂ at 300 K, as a function of **c** methanol-d₄ pressure (Pt_{uc}/Pt ratio 0.10) and **d** Pt_{uc} concentration (10⁻² mbar). In (b), the gray line denotes the spectrum, and the black one is the sum of fitted curves; CH_x⁺ and C⁺ signals are fitted with blue and purple lines, respectively. In **c** and **d**, the error bars indicate the reproducibility.

CD_xO^{*}, and CD_x^{*}; therefore, its formation as the major desorbing species reflects the essential role of dehydrogenation at different stages of methanol-d₄ decomposition. Both D₂O_(g) and CD_{4(g)} were possible products, reflecting the process of C-O bond scission, but they could not be resolved by our mass spectra. CD_{4(g)} was formed through CD_x^{*} combining with D^{*}, and D₂O_(g) through either O^{*} or OD^{*} combining with D^{*}. The observed CD₂O_(g) suggests that CH_xO^{*} decreased above 180 K (Fig. 3e) through not only C-O bond scission but also desorption as CH₂O_(g). The formation of CD₂O_(g) and D₂O_(g) also rationalizes scarce O^{*} remaining on the surface, as evidenced by vanishing O 1s signals above 200 K in the UHV PES experiments as well as absent O 1s signals in the NAP-PES spectra (300 K). The absence of CO_(g) and CO^{*} indicates that the dehydrogenation of methanol-d₄ (or methanol) to CO, a process typically observed on Pt clusters or single crystals^{22–24,26,30,33–36,42}, did not occur on the Pt_{uc}

sites of PtTe₂. The observed C^{*} accordingly originated from dehydrogenated CH_x^{*}.

The gaseous products also confirm that the reactivity and selectivity of Pt_{uc} sites depend on the Pt_{uc} concentration. Fig. 5d shows the gaseous products (at methanol pressure 10⁻² mbar) as a function of the Pt_{uc} concentration. For a Pt_{uc} concentration <20 %, the products increased generally with the Pt_{uc} concentration, which is consistent with the trend shown in Fig. 4a. The production of CD₂O_(g) dropped dramatically when the Pt_{uc} concentration increased above 20 %, in agreement with the decrease of CH_xO^{*} (Fig. 4a). The produced D_{2(g)} also decreased, indicating the selectively suppressed dehydrogenation to CH_xO^{*}. In contrast, CD_{4(g)}/D₂O_(g) decreased only slightly at a Pt_{uc} concentration > 20 %, as CD_x^{*} increased at 180 K (Fig. 4a); the proportion of CD_x^{*} desorbing as CD_{4(g)} could vary with the Pt_{uc} concentration. The dependence is associated, as discussed above, with the

composition of Pt_{uc}-Vac and Pt_{uc}-Ex evolving with the Pt_{uc} concentration.

DFT modeling

Our first-principles DFT modeling aimed to elucidate the key mechanisms behind the observed reactions. We established a Te-divacancy model by removing two adjacent Te atoms at the topmost layer in order to mimic a PtTe₂ surface at which the reactive sites consist primarily of the Te vacancies (Fig. 1b,e). The model is applicable to the cases of Pt_{uc} concentration ≤ 20 % because the Te vacancies remained as the main surface defects despite the growth of the Pt_{uc}-Ex at a Pt_{uc} concentration > 10 %. Although the Te vacancies of various sizes were observed, the divacancy model suffices to represent the key features of the reactions on the Pt_{uc}-Vac sites. A divacancy site has five Pt_{uc}-Vac: one loses two Te-Pt bonds in the bilayer structure (denoted as Pt_{uc2}-Vac), corresponding to the coordination to four Te, and the other four lose one Te-Pt bond (Pt_{uc1}-Vac), illustrated in Fig. 6a. The structural modeling confirms that the underlying Pt atoms remain nearly at the same positions after the removal of surface Te. We considered three main reaction processes in the methanol decomposition: dehydrogenation from either oxygen (red arrows) or carbon (green arrow), and C-O bond scission (deoxygenation and dihydroxylation; black arrows), presented in Fig. 6b. The adsorption configurations and energies of methanol and its decomposition fragments are presented in Fig. S5. The modeling shows that a methanol molecule adsorbs on a Pt_{uc}-Vac site with an O-Pt binding configuration and adsorption energy -1.02 eV, which is evidently stronger than that (-0.41 eV) on pristine PtTe₂ basal plane (Fig. S5). The Pt_{uc}-Vac, therefore, has the potential to serve as a reactive center on PtTe₂. The three main decomposition processes at varied stages at the divacancy sites were calculated and compared. For the first step of decomposition, the barrier for dehydrogenation from oxygen (0.66 eV) of CH₃OH* was significantly smaller than those for dehydrogenation from carbon (1.42 eV) and dehydroxylation (1.82 eV). The comparison suggests the preferential formation of methoxy (CH₃O*), agreeing well with the observed selectivity that methanol decomposed via a pathway to produce more CH_xO* than CH_x* at a small Pt_{uc} concentration (Fig. 4a). The great difference between the energy barriers for desorption and dehydrogenation to CH₃O* (1.02 vs. 0.66 eV) also explains the great conversion probability for methanol adsorbed on the Pt_{uc}-Vac site (Fig. 4b). CH₃O* is expected to undergo further dehydrogenation (with a barrier 1.08 eV) to formaldehyde (CH₂O*), because of the considerably greater activation energies for the two competing processes, namely desorption (2.58 eV) and deoxygenation (2.29 eV). CH₂O*, due to its planar structure with sp² hybridized carbons, has an adsorption energy (-1.52 eV) smaller than those of the other intermediates, that impedes subsequent decomposition. Compared to the greater barriers for its C-O bond cleavage (3.33 eV) or further dehydrogenation (to CHO*, 1.56 eV), CH₂O* would prefer desorption (as CH₂O_(g)) to decomposition at elevated temperature, as observed in our NAP-MS experiments (Fig. 5c, d). Alternatively, if H* from the dehydrogenation is nearby (not yet desorbed as H_{2(g)}), then CH₂O* could also combine with H* to form CH₂OH* (with a small barrier 0.12 eV), which provides a feasible pathway for further reactions. CH₂OH* would decompose via dehydroxylation to CH₂* and OH*, instead of dehydrogenation to CHO* and H*; the latter process does not occur because the inverse process (CHOH* + H* → CH₂OH*) has a negligible barrier (<0.01 eV) and CH₂OH* has a lower total energy. As the barrier for the dehydroxylation (1.27 eV) of CH₂OH* is evidently smaller than those for the C-O bond scission of CH₃O* and CH₂O* (2.29 and 3.33 eV), the observed CH_x species resulted from decomposed CH₂OH*. As a result, the observed CH_xO* species in our PES spectra correspond to CH₃O* and CH₂O* and the CH_x species mainly to CH₂* and CH₁*. The CH₂* species may undergo either further dehydrogenation to yield C* or combination with H* to produce CH_{4(g)}, as observed in NAP-PES spectra (Fig. 5a)

and NAP-MS spectra (Fig. 5c, d) respectively. Details of the calculated energy barriers are provided in our Supplementary Information (Figs. S5 – S18).

After the C-O bond scission of CH₂OH*, the produced OH* either diffuses away from the active sites or combines with H* to desorb as H₂O_(g) (Fig. 5c, d), so its “poisoning effect” is insignificant. The calculated activation energy for OH* to migrate to an intermediate adsorption site on Te at the edge of divacancy amounts to 0.95 eV; their diffusion barrier on the basal plane is even smaller (0.36 eV), as shown in Fig. S19. These diffusion barriers are smaller than that for the C-O bond scission of CH₂OH*, so with the progress of methanol decomposition, the produced OH* can diffuse readily to other sites to prevent the active sites from obstruction.

The above modeling shows that Pt_{uc}-Vac in the divacancy model activates the decomposition in a coordinative manner; the adsorbates (CH₃OH*, its decomposition intermediates and fragments) are bonded mostly to two or three Pt_{uc}-Vac in varied decomposition processes (Figs. S5 – S18). Fig. 7a shows the simulated dehydrogenation of CH₃OH* to CH₃O* as an example. CH₃OH* first adsorbs on the Pt_{uc2}-Vac through its O and then undergoes the scission of O-H bond. At the final stage, H* is bonded to one of Pt_{uc1}-Vac and CH₃O* to both Pt_{uc1}-Vac and Pt_{uc2}-Vac. It is noted that neither CH₃O* nor H* is bonded to Te near the vacancy in the process, since they adsorb weakly on these Te sites, like CH₃OH* and its other decomposition intermediates or fragments (Fig. S5). As Te atoms at PtTe₂ surface are mainly bonded to the underlying Pt^{6,11,55}, instead of their neighboring Te atoms, the removal of surface Te atoms altered little the electronic properties of Te atoms surrounding the vacancies — the bonding of these surface Te atoms remains saturated. As a result, they were not heavily involved in the methanol decomposition. In the divacancy model, Pt_{uc2}-Vac appears to be more active than Pt_{uc1}-Vac, indicating that the processes are mostly centered around Pt_{uc2}-Vac in spite of varied reaction pathways (Figs. S5 – S18). The Pt_{uc}-Vac are like separated Pt single atoms, triangularly positioned and oxidized to different extents dependent on their bonding to Te. The number of coordination (to Te) or missing Te-Pt bonds of Pt_{uc}-Vac determines its electronic properties and hence catalytic properties. To illuminate the effect of the coordination number of Pt_{uc}-Vac on the activity, a tri-vacancy model with a Pt_{uc3}-Vac in the middle of the tri-vacancy site, which was also likely formed on the Ar⁺-bombarded PtTe₂ surface, was introduced to simulate the reactions. The results show that the adsorption energies of CH₃OH*, CH₃O* and CH₂O* on the tri-vacancy site were slightly increased by 0.05–0.10 eV, and the energy barrier for dehydrogenation of CH₃OH* to CH₃O* remained similar, whereas that of CH₃O* to CH₂O* was reduced by 0.12 eV (Figs. S20–S22). Consequently, the formation of CH₂O* on this tri-vacancy became more probable. Reducing the coordination to Te enhances the activity of Pt_{uc}-Vac.

The corresponding electronic structures reflect the same trend. The measured and calculated local densities of states (LDOS) near the Fermi level of Pt_{uc0-3}-Vac (Fig. 7b) show consistently that with decreased coordination number, the Pt_{uc0-3}-Vac at PtTe₂ surface become more metallic, reflected on the enhanced LDOS near the Fermi level; meanwhile, their d-band centers shift toward higher energies (Fig. 7c). Both results are indicative of enhanced catalytic reactivity^{74,75}. The LDOS of Pt_{uc1-3}-Vac at PtTe₂ surface and Pt at Pt(111) surface are evidently different (Fig. S23), accounting for their different catalytic behaviors. Previous studies indicate that the spatial distribution and orientation of frontier orbitals of single-atom catalysts are well correlated with adsorption and catalytic activities⁷⁶. We note that the spatial distributions of frontier orbitals (in the energy ranging from -0.25 eV to the Fermi level) of Pt_{uc}-Vac at PtTe₂ surface expanded with decreased coordination number, as plotted in the insets of Fig. 7c. The expansion reflects a promoted probability of wave-function overlap, which is required for adsorption and catalytic activities⁷⁶, so agrees with the enhanced reactivity indicated above. Thus, the characteristic reactivity

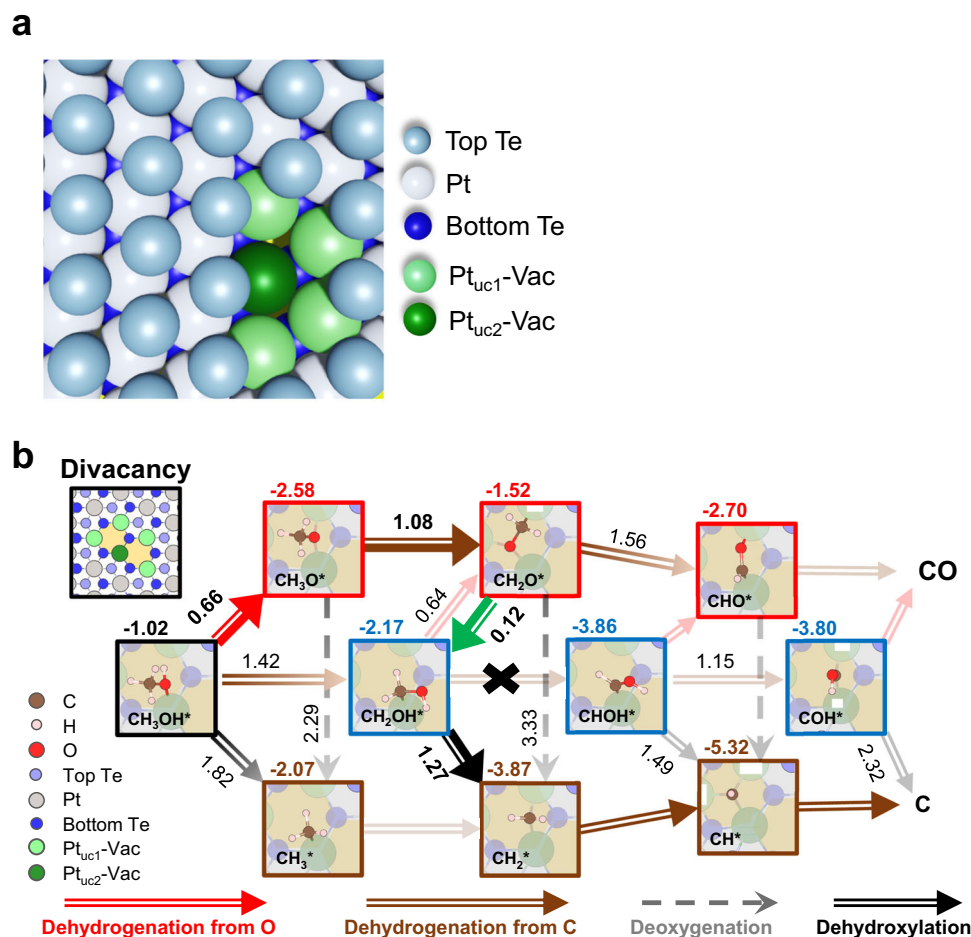


Fig. 6 | Schematic pathways of methanol reactions on a Te-divacancy site at PtTe₂ surface. a The atomic model for a Te divacancy at PtTe₂ surface. **b** Pathways of methanol decomposition on the Te-divacancy site at PtTe₂ surface. In **b**, the possible intermediates in their most stable configurations and their adsorption energies on the Te-divacancy site are presented (value at the upper-left corner of each panel). The sizes of Pt and Te atoms in the model are varied to illustrate their relative positions from top view. Brown and red hollow arrows indicate the

dehydrogenation process from C and O atoms of methanol, respectively; black hollow and grey dashed arrows represent dehydroxylation and deoxygenation processes, respectively; the green hollow arrow indicates a hydrogenation process. For clarity, the arrows for the most plausible processes in the methanol decomposition are enlarged. The value beside each arrow is provided for the energy barrier of the specific process.

of the Pt_{uc}-Vac arises from not only the peculiar structural (geometric) effect – triangularly positioned Pt_{uc}-Vac, but also the electronic effect – differently oxidized Pt_{uc}-Vac.

The above modeling also indicates that enlarging the Te vacancies (increasing the number of more active Pt_{uc3}-Vac) promotes the main reaction processes shown in Fig. 6b, instead of altering the reaction pathway. It accordingly supports the argument that a separated reaction pathway reflected on either the decreased conversion probability to CH_xO on Pt_{uc} sites (Fig. 4b) or the decreased production of CD₂O_(g) and D_{2(g)} (Fig. 5d) at a greater Pt_{uc} concentration was initiated by the Pt_{uc}-Ex. The Pt_{uc}-Ex consists largely of Pt_{uc} at the edges of PtTe₂ patches (Fig. 1c and S4b) or in redeposited Pt-Te nanoclusters (Fig. 1c). The Pt_{uc}-Ex at the edges of PtTe₂ patches (islands) are primarily the Pt_{uc} with one missing Te-Pt bond (Pt_{uc1}-Ex), as illustrated in Fig. S24. Our DFT modeling for methanol on the edges of PtTe₂ patches (Figs. S24–S27) show that CH₃OH* on the edge Pt_{uc1}-Ex sites prefers desorption to decomposition, in the light of evidently greater activation energies for the dehydrogenation to CH₃O* (1.64 eV) and the C-O bond scission (2.07 eV) than that for desorption (0.57 eV). Notably, the activation energies are greater and the adsorption is weaker than those (Fig. 6b and Fig. S20) on the Pt_{uc2}-Vac (or Pt_{uc3}-Vac) in the divacancies (trivacancies). The result implies that increasing the edge Pt_{uc1}-Ex sites decreases the average conversion probability (to both CH_xO* and

CH_x*) on Pt_{uc} sites, which explains the observed behavior of CH_xO* (Fig. 4b). As a result, the Pt_{uc}-Ex on the redeposited Pt-Te nanoclusters should be responsible for the production of CH_x*, to match the nearly constant probability of conversion to CH_x* (Fig. 4b). Earlier studies showed that the C-O bond scission of methanol and subsequent production of CH₄ were promoted on supported nanoscale Pt clusters³⁴; meanwhile, the dehydrogenation to CO also occurred, which contrasts with the present observation. Therefore, the Pt-Te nanoclusters, instead of pure Pt clusters, are more likely the structures to yield CH_x*. These Pt-Te nanoclusters had no long-range structural ordering since our RHEED measurements showed no additional diffraction patterns. As they were formed by nucleation of redeposited Pt and Te, the Pt atoms in the clusters were not bonded exclusively to Te so not separated as far as those in PtTe₂. The Pt_{uc}-Ex at the cluster's surface thus differs structurally from the Pt_{uc}-Vac and the Pt_{uc}-Ex at edges of PtTe₂ patches discussed above. Small Pt aggregates likely formed in the Pt-Te clusters so their surface Pt_{uc}-Ex exhibited reactivity partially resembling that of supported Pt nanoclusters³⁴.

Discussion

With STM, PES, NAP-PES, NAP-MS, and DFT calculations, we studied methanol reactions on layered PtTe₂ under both UHV and NAP (up to 0.1 mbar) conditions. A structurally perfect PtTe₂ surface was inactive

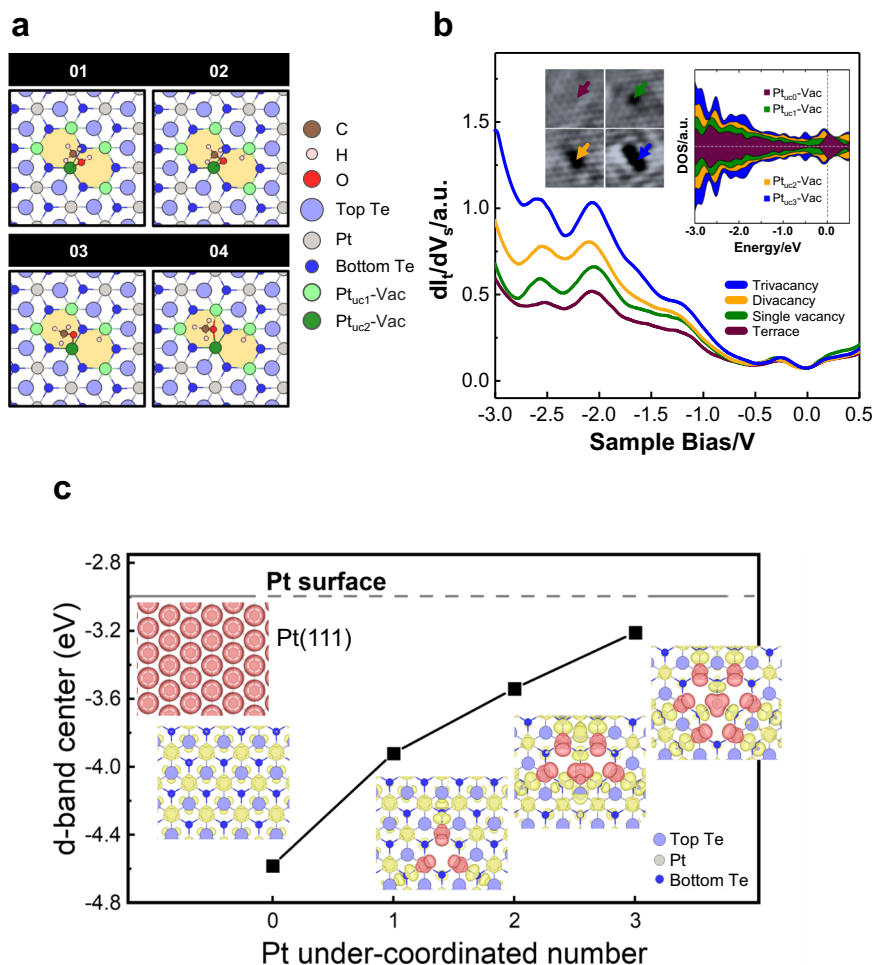


Fig. 7 | Dehydrogenation processes of CH_3OH^* to CH_3O^* on a Te-divacancy site and electronic structures near the Fermi level of $\text{Pt}_{\text{uc}}\text{-Vac}$. **a** Schematics illustrating the dehydrogenation processes (1 \rightarrow 4) of CH_3OH^* to CH_3O^* on a Te-divacancy site; the corresponding energy profile is given in Fig. S7. **b** Comparison of the measured and calculated (inset) LDOS near the Fermi level of $\text{Pt}_{\text{uc}0-3}\text{-Vac}$. **c** Comparison of d-band centers of $\text{Pt}_{\text{uc}}\text{-Vac}$ at PtTe_2 surface and Pt at Pt(111) surface. In **b**, the measurements, dI_t/dV_g vs. V_s , were conducted with scanning

tunneling spectroscopy (STS), the arrows in the STM images (inset) indicate the locations where the STS measurements were performed, and the dash line in the calculated LDOS (inset) indicates the Fermi level. In **c**, the Pt under-coordination number, the x-axis, indicates the number of missing Te-Pt bonds of $\text{Pt}_{\text{uc}}\text{-Vac}$. The insets show the corresponding spatial distributions of frontier orbitals (in the energy ranging from -0.25 eV to the Fermi level) of $\text{Pt}_{\text{uc}}\text{-Vac}$ (red spheres), the other atoms (yellow) at PtTe_2 surface, and Pt at Pt(111) surface (red).

whereas the surface with Pt_{uc} sites, which was formed primarily by removing surface Te using controlled Ar^+ bombardment, became able to activate methanol decomposition. Adsorbed methanol on the $\text{Pt}_{\text{uc}}\text{-Vac}$ sites, the dominating reactive sites at small Pt_{uc} concentrations, began to decompose at approximately 160 K and yielded CH_xO^* ($x = 2$ and 3) as the main intermediates; CH_xO^* either desorbed as $\text{CH}_2\text{O}_{(\text{g})}$ or decomposed further, via the transient formation and subsequent C-O bond scission of CH_2OH^* , to produce CH_x^* ($x = 1$ and 2). The reaction probability on the $\text{Pt}_{\text{uc}}\text{-Vac}$ sites exceeded 90 % — approximately 60 % of the methanol decomposed to CH_xO^* and 35 % to CH_x^* at 180 K, and the reaction ultimately produced gaseous hydrogen, methane, water, and formaldehyde at elevated temperature. We argue that the $\text{Pt}_{\text{uc}}\text{-Vac}$ activated the reaction processes like single-atom catalysts and in a coordinative manner; their triangular positioning and varied degrees of oxidation accounted for the observed characteristic reactivity. Increased Ar^+ dosage (Pt_{uc} concentration increased to 10 – 20 %) generated structurally different $\text{Pt}_{\text{uc}}\text{-Ex}$, associated with the edges of PtTe_2 patches and re-deposited Pt-Te nanoclusters, even though the Te vacancies remained major at the surface; on such $\text{Pt}_{\text{uc}}\text{-Ex}$ sites the probability of decomposition to CH_xO^* was selectively decreased. A consistent trend was reflected in the gaseous products from the reaction under NAP conditions. The results suggest that the PtTe_2

surface can serve as a superior catalyst toward methanol decomposition, with advantages of great catalytic reactivity and tunable selectivity.

Methods

Sample preparation

Single-crystal PtTe_2 was synthesized by the self-flux method. High-purity Pt (99.99%, 0.35 g, 1.79 mmol) foils and a Te ingot (99.9999%, 4.35 g, 34.09 mmol), obtained from Ultimate Materials Technology Co., Ltd, were mixed in a ratio of 1:17 and sealed in a quartz tube under vacuum at $\sim 5 \times 10^{-5}$ Torr. The tube was heated to 1000 °C in 12 hours, held there for 24 hours, and then slowly cooled to 500 °C at a rate of -3 to -5 °C. The excess Te was subsequently separated by centrifugation. To improve the crystal quality and remove any residual Te, the crystal was sealed in an evacuated quartz tube again and heated at 450 °C for 100 hours. The average yield of PtTe_2 with this method was 90 – 95% (based on Pt). The grown bulk crystal has a diameter near 8.0 mm; it was cleaved in situ before each experiment.

Characterization

The UHV experiments were conducted in UHV chambers with a base pressure in the regime of 10^{-10} Torr. Ar^+ bombardment was performed

with an acceleration energy of 0.5–2.0 keV and under a pressure of 5×10^{-6} Torr; 0.5 keV was chosen for the sample preparation in catalytic studies. The sample was maintained at 300 K for exposure to CH₃OH and methanol-d₄ (CD₃OD) at selected pressures. The highly pure CH₃OH and CD₃OD (Merck, 99.8%) were additionally purified by repeated freeze–pump–thaw cycles before being introduced into the experimental chambers. The gas exposure in the present work is reported in Langmuir units ($1.0 \text{ L} = 1 \times 10^{-6} \text{ Torr s}$). STM images were acquired at sample temperature 77 K (samples cooled from 300 K in an hour) in constant-current mode using an electrochemically etched tungsten tip, with a sample bias voltage (V_s) of –150 mV – –500 mV and a tunneling current (I_t) of 1.0–3.0 nA. The PES and NAP-PES experiments were conducted at the TLS BL09A2 and BL24A beamlines, respectively, at the National Synchrotron Radiation Research Center (NSRRC) in Taiwan^{77,78}. For the former, the incident photon beam (with a fixed energy 410 eV) was normal to the surface and photoelectrons were collected (Scienta R3000) at an angle of 58° from the surface normal; for the latter, the beam (with a fixed energy 380 eV) was incident 56° from the surface normal and the analyzer (SPECS NAP 150), equipped with a 4-stages differential pumping system, was placed normal to the surface. The energy resolution was estimated to be near 0.1 eV and the BE was referred to the Au 4f core level at 84.0 eV of an Au substrate placed beside the investigated PtTe₂ sample. All spectra presented here were normalized to the photon flux. The gaseous reaction products were measured with NAP-MS, comprised of a quadrupole mass spectrometer (Hiden HAL201RC) and a doubly-differentially pumping system with a stainless steel tubing inlet terminated with an aperture (a diameter 0.75 mm) 3 mm from the sample. We used a full-range gauge mounted on the reaction chamber to calibrate the ion current at a selected m/z ratio to the partial pressure of the corresponding product. The presented partial pressures of the gaseous products were derived by subtracting the background, which was collected from as-cleaved PtTe₂ surface (inert toward methanol decomposition), under the corresponding methanol pressure.

DFT calculations

First-principles calculations were performed by using Vienna ab initio simulation package (VASP)^{79,80}, in the framework of DFT with the projector-augmented wave (PAW) method⁸¹ and the Perdew–Burke–Ernzerhof functional⁸² type generalized gradient approximation exchange–correlation functional. For the 1T-PtTe₂ calculations, the energy cutoff was 330 eV and the energy convergence criterion was 10^{-4} eV. A $12 \times 12 \times 1$ Γ -centered k-point sampling was performed for the Brillouin zone integration until the relative energies converged to a few meV. The optimized lattice constant was 3.91 Å, in good agreement with a previous report of 3.9 Å⁸³. We included weak van der Waals (vdW) interaction between adjacent two bilayers using the recently developed SCAN+rVV10⁸⁴ correction method that yielded excellent geometric and energetic results at a reasonable computational cost. The 1T-PtTe₂ layered structure was then modeled by a 6×6 supercell with three bilayers of 1T-PtTe₂. The bottom bilayer was fixed and the remaining two bilayers were allowed to relax. The adsorption energy (E_{ads}) for each adsorbate was evaluated by the following standard formula: $E_{\text{ads}} = E_{\text{A}+\text{S}} - E_{\text{S}} - E_{\text{A}}$, where $E_{\text{A}+\text{S}}$, E_{S} , and E_{A} denote the total energies of the adsorbed system, the clean PtTe₂ layered system, and the chemical potentials of the corresponding adsorbed species in a gas phase, respectively. The energy barriers were determined using the climbing image nudged elastic band (CINEB) method⁸⁵.

Data availability

Data that support the findings of this study are presented in the main article and Supplementary Information files. Source data are provided with this paper.

Code availability

DFT simulations were performed by using The Vienna Ab initio Simulation Package (VASP)^{79,80}.

References

1. Yan, M. et al. Lorentz-violating type-II Dirac fermions in transition metal dichalcogenide PtTe₂. *Nat. Commun.* **8**, 257 (2017).
2. Oyedele, A. D. et al. PdSe₂: pentagonal two-dimensional layers with high air stability for electronics. *J. Am. Chem. Soc.* **139**, 14090–14097 (2017).
3. Ma, H. et al. Thickness-tunable synthesis of ultrathin type-II Dirac semimetal PtTe₂ single crystals and their thickness-dependent electronic properties. *Nano Lett.* **18**, 3523–3529 (2018).
4. Bahramy, M. S. et al. Ubiquitous formation of bulk Dirac cones and topological surface states from a single orbital manifold in transition-metal dichalcogenides. *Nat. Mater.* **17**, 21–28 (2018).
5. Ghosh, B. et al. Broadband excitation spectrum of bulk crystals and thin layers of PtTe₂. *Phys. Rev. B* **99**, 045414 (2019).
6. Politano, A. et al. 3D Dirac plasmons in the type-II Dirac semimetal PtTe₂. *Phys. Rev. Lett.* **121**, 086804 (2018).
7. Lin, M.-K. et al. Dimensionality-mediated semimetal–semiconductor transition in ultrathin PtTe₂ films. *Phys. Rev. Lett.* **124**, 036402 (2020).
8. D’Olimpio, G. et al. PdTe₂ transition-metal dichalcogenide: chemical reactivity, thermal stability, and device implementation. *Adv. Funct. Mater.* **30**, 1906556 (2020).
9. Xie, J. et al. Controllable disorder engineering in oxygen-incorporated MoS₂ ultrathin nanosheets for efficient hydrogen evolution. *J. Am. Chem. Soc.* **135**, 17881–17888 (2013).
10. Li, H. et al. Corrigendum: activating and optimizing MoS₂ basal planes for hydrogen evolution through the formation of strained sulphur vacancies. *Nat. Mater.* **15**, 364 (2016).
11. Politano, A. et al. Tailoring the Surface Chemical Reactivity of Transition-Metal Dichalcogenide PtTe₂ Crystals. *Adv. Funct. Mater.* **28**, 1706504 (2018).
12. Chen, Y. et al. Tuning electronic structure of single layer MoS₂ through defect and interface engineering. *ACS Nano* **12**, 2569–2579 (2018).
13. Yang, J. et al. Single atomic vacancy catalysis. *ACS Nano* **13**, 9958–9964 (2019).
14. Wang, X. et al. Single-atom vacancy defect to trigger high-efficiency hydrogen evolution of MoS₂. *J. Am. Chem. Soc.* **142**, 4298–4308 (2020).
15. Hu, J. et al. Sulfur vacancy-rich MoS₂ as a catalyst for the hydrogenation of CO₂ to methanol. *Nat. Catal.* **4**, 242–250 (2021).
16. Xu, J. et al. Frenkel-defected monolayer MoS₂ catalysts for efficient hydrogen evolution. *Nat. Commun.* **13**, 2193 (2022).
17. Xie, J. et al. Defect-rich MoS₂ ultrathin nanosheets with additional active edge sites for enhanced electrocatalytic hydrogen evolution. *Adv. Mater.* **25**, 5807–5813 (2013).
18. Nan, H. et al. Strong photoluminescence enhancement of MoS₂ through defect engineering and oxygen bonding. *ACS Nano* **8**, 5738–5745 (2014).
19. He, Z. et al. Defect engineering in single-layer MoS₂ using heavy ion irradiation. *ACS Appl. Mater. Interfaces* **10**, 42524–42533 (2018).
20. Du, H.-Y. et al. Nanoscale redox mapping at the MoS₂–liquid interface. *Nat. Commun.* **12**, 1321 (2021).
21. Huang, Y.-F. et al. Thickness-dependent photocatalysis of ultra-thin MoS₂ film for visible-light-driven CO₂ reduction. *Catalysts* **11**, 1295 (2021).
22. Sexton, B. A. Methanol decomposition on platinum (111). *Surf. Sci.* **102**, 271–281 (1981).
23. Sexton, B. A., Rendulic, K. D. & Huges, A. E. Decomposition pathways of C₁–C₄ alcohols adsorbed on platinum (111). *Surf. Sci.* **121**, 181–198 (1982).

24. Akhter, S. & White, J. M. A static SIMS/TPD study of the kinetics of methoxy formation and decomposition on O/Pt(111). *Surf. Sci.* **167**, 101–126 (1986).
25. Attard, G. A., Chibane, K., Ebert, H. D. & Parsons, R. The adsorption and decomposition of methanol on Pt(110). *Surf. Sci.* **224**, 311–326 (1989).
26. Gibson, K. D. & Dubois, L. H. Step effects in the thermal decomposition of methanol on Pt(111). *Surf. Sci.* **233**, 59–64 (1990).
27. Wang, J. & Masel, R. I. Carbon-oxygen bond scission during methanol decomposition on (1 × 1)platinum(110). *J. Am. Chem. Soc.* **113**, 5850–5856 (1991).
28. Franaszczuk, K. et al. A comparison of electrochemical and gas-phase decomposition of methanol on platinum surfaces. *J. Phys. Chem.* **96**, 8509–8516 (1992).
29. Kizhakevariam, N. & Stuve, E. M. Promotion and poisoning of the reaction of methanol on clean and modified platinum (100). *Surf. Sci.* **286**, 246–260 (1993).
30. Greeley, J. & Mavrikakis, M. Competitive paths for methanol decomposition on Pt(111). *J. Am. Chem. Soc.* **126**, 3910–3919 (2004).
31. Antolini, E., Salgado, J. R. C. & Gonzalez, E. R. The methanol oxidation reaction on platinum alloys with the first row transition metals: The case of Pt–Co and –Ni alloy electrocatalysts for DMFCs: a short review. *Appl. Catal. B: Environ.* **63**, 137–149 (2006).
32. Peng, T. L. & Bernasek, S. L. The internal energy of CO₂ produced by the catalytic oxidation of CH₃OH by O₂ on polycrystalline platinum. *J. Chem. Phys.* **131**, 154701 (2009).
33. Matolínová, I. et al. CO and methanol adsorption on (2 × 1)Pt(110) and ion-eroded Pt(111) model catalysts. *Surf. Interface Anal.* **43**, 1325–1331 (2011).
34. Chao, C.-S. et al. Two-channel decomposition of methanol on Pt nanoclusters supported on a thin film of Al₂O₃/NiAl(100). *J. Phys. Chem. C* **117**, 5667–5677 (2013).
35. Miller, A. V., Kaichev, V. V., Prosvirin, I. P. & Bukhtiyarov, V. I. Mechanistic study of methanol decomposition and oxidation on Pt(111). *J. Phys. Chem. C* **117**, 8189–8197 (2013).
36. Wang, H. et al. In situ XANES study of methanol decomposition and partial oxidation to syn-gas over supported Pt catalyst on SrTiO₃ nanocubes. *Catal. Today* **237**, 71–79 (2014).
37. Kemppainen, E. et al. Scalability and feasibility of photoelectrochemical H₂ evolution: the ultimate limit of Pt nanoparticle as an HER catalyst. *Energy Environ. Sci.* **8**, 2991–2999 (2015).
38. Kattel, S., Yan, B., Chen, J. G. & Liu, P. CO₂ hydrogenation on Pt, Pt/SiO₂ and Pt/TiO₂: importance of synergy between Pt and oxide support. *J. Catal.* **343**, 115–126 (2016).
39. Lin, L. et al. Low-temperature hydrogen production from water and methanol using Pt/α-MoC catalysts. *Nature* **544**, 80–83 (2017).
40. Li, H. et al. Synergetic interaction between neighbouring platinum monomers in CO₂ hydrogenation. *Nat. Nanotechnol.* **13**, 411–417 (2018).
41. Damte, J. Y., Lyu, S.-I., Leggesse, E. G. & Jiang, J. C. Methanol decomposition reactions over a boron-doped graphene supported Ru–Pt catalyst. *Phys. Chem. Chem. Phys.* **20**, 9355–9363 (2018).
42. Liao, T.-W. et al. Composition-tuned Pt-skinned ptini bimetallic clusters as highly efficient methanol dehydrogenation catalysts. *Chem. Mater.* **31**, 10040–10048 (2019).
43. Chia, X. et al. Layered platinum dichalcogenides (PtS₂, PtSe₂, and PtTe₂) electrocatalysis: monotonic dependence on the chalcogen size. *Adv. Funct. Mater.* **26**, 4306–4318 (2016).
44. Chia, X., Sofer, Z., Luxa, J. & Pumera, M. Layered noble metal dichalcogenides: tailoring electrochemical and catalytic properties. *ACS Appl. Mater. Interfaces* **9**, 25587–25599 (2017).
45. Li, X. et al. Ordered clustering of single atomic Te vacancies in atomically thin PtTe₂ promotes hydrogen evolution catalysis. *Nat. Commun.* **12**, 2351 (2021).
46. Burstein, G. T., Barnett, C. J., Kucernak, A. R. & Williams, K. R. Aspects of the anodic oxidation of methanol. *Catal. Today* **38**, 425–437 (1997).
47. Hamnett, A. Mechanism and electrocatalysis in the direct methanol fuel cell. *Catal. Today* **38**, 445–457 (1997).
48. Williams, K. R. & Burstein, G. T. Low temperature fuel cells: Interactions between catalysts and engineering design. *Catal. Today* **38**, 401–410 (1997).
49. Aricò, A. S., Srinivasan, S. & Antonucci, V. DMFCs: from fundamental aspects to technology development. *Fuel Cells* **1**, 133–161 (2001).
50. Rostrup-Nielsen, J. R. Fuels and energy for the future: the role of catalysis. *Catal. Rev.* **46**, 247–270 (2004).
51. Li, X. & Faghri, A. Review and advances of direct methanol fuel cells (DMFCs) part I: Design, fabrication, and testing with high concentration methanol solutions. *J. Power Sources* **226**, 223–240 (2013).
52. Bahrami, H. & Faghri, A. Review and advances of direct methanol fuel cells: Part II: Modeling and numerical simulation. *J. Power Sources* **230**, 303–320 (2013).
53. Peraldo Bicelli, L. Hydrogen: a clean energy source. *Int. J. Hydrog. Energy* **11**, 555–562 (1986).
54. Hung, Y.-H. et al. Manipulation of heteroatom substitution on nitrogen and phosphorus co-doped graphene as a high active catalyst for hydrogen evolution reaction. *J. Phys. Chem. C* **123**, 22202–22211 (2019).
55. Zhussupbekov, K. et al. Imaging and identification of point defects in PtTe₂. *npj 2D Mater. Appl.* **5**, 14 (2021).
56. Hu, G.-R. et al. Low-temperature decomposition of methanol on Au nanoclusters supported on a thin film of Al₂O₃/NiAl(100). *Phys. Chem. Chem. Phys.* **13**, 3281–3290 (2011).
57. Hung, T.-C. et al. Dependence on size of supported rh nanoclusters in the decomposition of methanol. *ACS Catal.* **5**, 4276–4287 (2015).
58. Cox, D. F. & Schulz, K. H. Methanol decomposition on single crystal Cu₂O. *J. Vac. Sci. Technol. A* **8**, 2599–2604 (1990).
59. Bukhtiyarov, V. I. et al. In situ study of selective oxidation of methanol to formaldehyde over copper. *React. Kinet. Catal. Lett.* **79**, 181–188 (2003).
60. Pöllmann, S., Bayer, A., Ammon, C. & Steinrück, H.-P. Adsorption and reaction of methanol on clean and oxygen precovered Cu(111). *Z. f.ür. Physikalische Chem.* **218**, 957–971 (2004).
61. Koitaya, T. et al. Systematic study of adsorption and the reaction of methanol on three model catalysts: Cu(111), Zn–Cu(111), and Oxidized Zn–Cu(111). *J. Phys. Chem. C* **121**, 25402–25410 (2017).
62. Besharat, Z. et al. Dehydrogenation of methanol on Cu₂O(100) and (111). *J. Chem. Phys.* **146**, 244702 (2017).
63. Setvin, M. et al. Methanol on anatase TiO₂ (101): mechanistic insights into photocatalysis. *ACS Catal.* **7**, 7081–7091 (2017).
64. Evans, P. E. et al. Methoxy formation induced defects on MoS₂. *J. Phys. Chem. C* **122**, 10042–10049 (2018).
65. Larciprete, R., Goldoni, A., Grošo, A., Lizzit, S. & Paolucci, G. The photochemistry of CH₄ adsorbed on Pt(111) studied by high resolution fast XPS. *Surf. Sci.* **482–485**, 134–140 (2001).
66. Fuhrmann, T. et al. Activated adsorption of methane on Pt(111)—an in situ XPS study. *N. J. Phys.* **7**, 107–107 (2005).
67. Hsia, Y.-Y. et al. Effects of O₂ and H₂O in the oxidative steam-reforming reaction of ethanol on Rh catalysts. *J. Phys. Chem. C* **123**, 11649–11661 (2019).
68. Wu, Y.-C. et al. Catalyzed decomposition of methanol-d₄ on vanadium nanoclusters supported on an ultrathin film of Al₂O₃/NiAl(100). *J. Phys. Chem. C* **126**, 3903–3914 (2022).
69. Liu, Z.-P. & Hu, P. General rules for predicting where a catalytic reaction should occur on metal surfaces: a density functional theory study of C–H and C–O bond breaking/making on flat, stepped,

- and kinked metal surfaces. *J. Am. Chem. Soc.* **125**, 1958–1967 (2003).
70. Van Santen, R. A. Complementary structure sensitive and insensitive catalytic relationships. *Acc. Chem. Res.* **42**, 57–66 (2009).
 71. van den Berg, R. et al. Structure sensitivity of Cu and CuZn catalysts relevant to industrial methanol synthesis. *Nat. Commun.* **7**, 13057 (2016).
 72. Freund, H. J. et al. Bridging the pressure and materials gaps between catalysis and surface science: clean and modified oxide surfaces. *Top. Catal.* **15**, 201–209 (2001).
 73. Liao, G.-J. et al. Decomposition of methanol-d₄ on a thin film of Al₂O₃/NiAl(100) under near-ambient-pressure conditions. *J. Chem. Phys.* **158**, 174707 (2023).
 74. Hammer, B. & Nørskov, J. K. Theoretical surface science and catalysis—calculations and concepts. In: *Advances in Catalysis*. Academic Press (2000).
 75. Wang, J.-H., Lee, C. S. & Lin, M. C. Mechanism of ethanol reforming: theoretical foundations. *J. Phys. Chem. C.* **113**, 6681–6688 (2009).
 76. Fu, Z., Yang, B. & Wu, R. Understanding the activity of single-atom catalysis from frontier orbitals. *Phys. Rev. Lett.* **125**, 156001 (2020).
 77. Hong, I. H. et al. Performance of the SRRC scanning photoelectron microscope. *Nucl. Instrum. Methods Phys. Res. Sect. A: Accelerators, Spectrometers, Detect. Associated Equip.* **467–468**, 905–908 (2001).
 78. Wang, C.-H., Chang, S.-T., Chen, S.-Y. & Yang, Y.-W. New ambient pressure X-ray photoelectron spectroscopy endstation at Taiwan light source. *AIP Conf. Proc.* **2054**, 040012 (2019).
 79. Kresse, G. & Furthmüller, J. Efficient iterative schemes for ab initio total-energy calculations using a plane-wave basis set. *Phys. Rev. B* **54**, 11169–11186 (1996).
 80. Kresse, G. & Furthmüller, J. Efficiency of ab-initio total energy calculations for metals and semiconductors using a plane-wave basis set. *Computational Mater. Sci.* **6**, 15–50 (1996).
 81. Blöchl, P. E. Projector augmented-wave method. *Phys. Rev. B* **50**, 17953–17979 (1994).
 82. Perdew, J. P., Burke, K. & Ernzerhof, M. Generalized gradient approximation made simple. *Phys. Rev. Lett.* **77**, 3865–3868 (1996).
 83. Hao, S. et al. Low-temperature eutectic synthesis of ptte₂ with weak antilocalization and controlled layer thinning. *Adv. Funct. Mater.* **28**, 1803746 (2018).
 84. Peng, H., Yang, Z.-H., Perdew, J. P. & Sun, J. Versatile van der waals density functional based on a meta-generalized gradient approximation. *Phys. Rev. X* **6**, 041005 (2016).
 85. Henkelman, G., Uberuaga, B. P. & Jónsson, H. A climbing image nudged elastic band method for finding saddle points and minimum energy paths. *J. Chem. Phys.* **113**, 9901–9904 (2000).

Acknowledgements

The National Science and Technology Council in Taiwan provided support with Grants No. NSTC 109-2112-M-018-008-MY3 (P.-H. C. and C.-P. C.), MOST 109-2112-M-008-030-MY2 (J.-W. H., L.-H. K. and M.-F. L.), NSTC 110-2112-M-213-010 (Y.-L. L. and Y.-J. H.), NSTC 110-2112-M-A49-013-MY3 (W.-H. Chen, C.-Y. C. and C.-L. L.), NSTC 110-2112-M-A49-022-MY2 (W.-H. Chen, C.-Y. C. and C.-L. L.), NSTC 111-2634-F-A49-008 (W.-H. Chen, C.-Y. C. and C.-L. L.), NSTC 112-2112-M-213-017 (C.-H. W.) and NSTC 112-2124-M-006-009 (C.-N. K. and C.-S. L.) for this work. This work

is also partially supported by the “Center for the Semiconductor Technology Research” from The Featured Areas Research Center Program within the framework of the Higher Education Sprout Project by the Ministry of Education in Taiwan. CPU time at Taiwan’s National Center for High-performance Computing (NCHC) is greatly appreciated. We also thank Drs. Hung-Wei Shiu and An-Cheng Yang for their technical support.

Author contributions

M.-F. L., C.-L. L., and J.-P. C. conceived and supervised the project. J.-W. H. and L.-H. K. performed measurements of PES, NAP-PES, NAP-MS, and RHEED, and analyzed the data. Y.-L. L., B.-H. L., C.-H. W. and Y.-J. H. assisted the synchrotron-based experiments. C.-N. K. and C.-S. L. prepared the TMDs samples. W.-H. C. and Q.-Y. Z. performed STM characterization. P.-H. C. and J.-P. C. performed DFT calculations. The text was initially composed by J.-W. H. and M.-F. L., with input from all co-authors. All authors further contributed to the discussion of the experimental work and the final version of the manuscript.

Competing interests

The authors declare no competing interests.

Additional information

Supplementary information The online version contains supplementary material available at <https://doi.org/10.1038/s41467-024-44840-z>.

Correspondence and requests for materials should be addressed to Chun-Liang Lin, Jyh-Pin Chou or Meng-Fan Luo.

Peer review information *Nature Communications* thanks the anonymous reviewers for their contribution to the peer review of this work. A peer review file is available.

Reprints and permissions information is available at <http://www.nature.com/reprints>

Publisher’s note Springer Nature remains neutral with regard to jurisdictional claims in published maps and institutional affiliations.

Open Access This article is licensed under a Creative Commons Attribution 4.0 International License, which permits use, sharing, adaptation, distribution and reproduction in any medium or format, as long as you give appropriate credit to the original author(s) and the source, provide a link to the Creative Commons licence, and indicate if changes were made. The images or other third party material in this article are included in the article’s Creative Commons licence, unless indicated otherwise in a credit line to the material. If material is not included in the article’s Creative Commons licence and your intended use is not permitted by statutory regulation or exceeds the permitted use, you will need to obtain permission directly from the copyright holder. To view a copy of this licence, visit <http://creativecommons.org/licenses/by/4.0/>.

© The Author(s) 2024